



Deposited via The University of Sheffield.

White Rose Research Online URL for this paper:

<https://eprints.whiterose.ac.uk/id/eprint/202187/>

Version: Published Version

---

**Article:**

Levano Blanch, O., Pope, J., Violatos, I. et al. (2023) Residual stress distributions in dissimilar titanium alloy diffusion bonds produced from powder using field-assisted sintering technology (FAST-DB). *Metallurgical and Materials Transactions A*, 54 (9). pp. 3578-3593. ISSN: 1073-5623

<https://doi.org/10.1007/s11661-023-07115-8>

---

**Reuse**

This article is distributed under the terms of the Creative Commons Attribution (CC BY) licence. This licence allows you to distribute, remix, tweak, and build upon the work, even commercially, as long as you credit the authors for the original work. More information and the full terms of the licence here:

<https://creativecommons.org/licenses/>

**Takedown**

If you consider content in White Rose Research Online to be in breach of UK law, please notify us by emailing [eprints@whiterose.ac.uk](mailto:eprints@whiterose.ac.uk) including the URL of the record and the reason for the withdrawal request.



# Residual Stress Distributions in Dissimilar Titanium Alloy Diffusion Bonds Produced From Powder Using Field-Assisted Sintering Technology (FAST-DB)

OLIVER LEVANO BLANCH, JACOB POPE, IOANNIS VIOLATOS, SALAHEDDIN RAHIMI, and MARTIN JACKSON

The conventional approach when engineering components manufactured from titanium is to design the thermomechanical processing to develop an optimal microstructure in a single alloy. However, this conventional approach can lead to unnecessary over-engineering of components, particularly when only a specific subcomponent region is under demanding service stresses and environments. One approach being developed to join multiple alloys in a single component and enhance engineering performance and efficiency is FAST-DB—whereby multiple alloys in powder form are diffusion bonded (DB) using field-assisted sintering technology (FAST). But the joining of multiple alloys using conventional welding and joining techniques can generate high residual stress in the bond region that can affect the mechanical performance of the components. In this study, the residual stress distribution across dissimilar titanium alloy diffusion bonds, processed from powder using FAST, were measured using X-Ray diffraction and the Contour method. The measurements show low residual stress in the bulk material processed with FAST as well as in the diffusion bond region. In addition, FAST-DB preforms subsequently hot forged into different near-net shapes were also analyzed to understand how the residual stress in the bond region is affected by a subsequent processing. Overall, no sharp transitions in residual stress was observed between the dissimilar alloys. This study reinforces confidence in the solid-state FAST process for manufacturing next generation components from multiple titanium alloy powders.

<https://doi.org/10.1007/s11661-023-07115-8>

© The Author(s) 2023

## I. INTRODUCTION

TITANIUM alloys are widely used for critical components in the aerospace sector due to their exceptional strength-to-weight ratio, corrosion and temperature resistance.<sup>[1–4]</sup> For example, approximately 25 to 30 pct of the weight of a gas turbine aero-engine is made up of titanium alloys.<sup>[2]</sup> Many titanium alloy components in an aero-engine require a good combination of creep and fatigue properties. Conventionally, as such components which include blades and discs in the compressor

section, are produced from a single forged billet of a particular alloy, such as Ti-6Al-4 V (Ti-64), Ti-6Al-2Sn-4Zr-6Mo (Ti-6246) and Ti-6Al-2Sn-4Zr-2Mo (Ti-6242), a compromise in properties is often required. For example, a compressor blade requires excellent creep resistance in the aerofoil and fatigue resistance in the root, yet the blade is closed die forged from the same bar stock that derives from a vacuum–arc remelted ingot. From a design standpoint, a multi-titanium alloy solution would optimize the performance of such components, whereby a more creep resistant titanium alloy (such as Ti-6242) in the root section is functionally graded or bonded into a more fatigue resistant alloy (such as Ti-6246) in the aerofoil subcomponent section. Similar examples exist in different parts of the airframe where the bonding of high strength, metastable  $\beta$  alloys such as Ti-5Al-5V-5Mo-3Cr (Ti-5553) to the more common and leaner alloys, such as Ti-64 or commercially pure (CP-Ti) grades. The ability to accurately bond or functionally grade without degrading the structural integrity of critical components would be disruptive technology that would enable designers to optimize key components and systems.

---

OLIVER LEVANO BLANCH, JACOB POPE, IOANNIS VIOLATOS, MARTIN JACKSON are with the Department of Materials Science and Engineering, The University of Sheffield, Mappin Street, Sheffield S1 3JD, UK. Contact e-mail: o.levano@sheffield.ac.uk SALAHEDDIN RAHIMI is with the Advanced Forming Research Centre (AFRC), University of Strathclyde, 85 Inchinnan Drive, Inchinnan, Renfrewshire PA4 9LJ, UK

Manuscript submitted February 15, 2023; accepted June 12, 2023.

Article published online June 25, 2023

Powder metallurgy approaches have been demonstrated to be a potential method for creating multi-material components. This is due to the flexibility of being able to distribute different powder feedstock in each sub region of a mold. Some of the most common powder metallurgy techniques are: Hot Pressing (HP), Hot Isostatic Pressing (HIP) and Field-Assisted Sintering Technology (FAST) or Spark Plasma Sintering (SPS). There have been several studies on the joining of Ti-Al with Ti-Al and Ti-64 with the technology HP<sup>[5-9]</sup> and HIP,<sup>[10,11]</sup> but these studies did not use powder feedstock. There have been a few studies that use FAST to diffusion bond (DB) or join two titanium alloys.<sup>[12-15]</sup> He *et al.*<sup>[12]</sup> made a comparison between FAST and HP showing that the strength of the bond is much higher in FAST material. Pope *et al.*<sup>[13]</sup> used the FAST-forging method<sup>[16]</sup> to create a near net shaped component made of two dissimilar titanium alloys (termed FAST-DB). Additionally, Pope *et al.*<sup>[14]</sup> demonstrated the strength in the bond of multiple combination of titanium alloys joined by FAST-DB. The strength of the FAST-DB bonds has also been demonstrated by Levano *et al.*<sup>[17,18]</sup> Titanium joints processed using HIP technology have also been shown to have good mechanical properties.<sup>[19]</sup>

The joining of two different alloys can potentially create chemical, thermal or mechanical strain misfits between the two materials which can introduce residual stresses in the bond.<sup>[20,21]</sup> Residual stresses are retained stresses inside a component when no external stress is applied. These stresses can have a direct impact on the mechanical properties and service performance of a component. Under fatigue loading, a component with high magnitudes of tensile residual stress will fail under lower number of cycles than the same component with low inherent residual stress from the manufacturing process.<sup>[2,22]</sup> However, there is an improvement in the fatigue life of the component in the presence of near surface compressive residual stresses, as such stresses oppose the initiation and opening of surface cracks.<sup>[2,22-26]</sup> Fairfax *et al.*<sup>[27]</sup> showed that from 147 residual stress induced failure cases analyzed, 55 of these involved some type of joint or bond. Therefore, it is essential to understand the generation of residual stress when developing new joining and diffusion bonding processes.

Two of the most common joining techniques in the aerospace sector are electron beam welding (EBW) and linear friction welding (LFW). Nevertheless, significant levels of residual stress can be generated in the weld when joining titanium alloys with EBW<sup>[28-30]</sup> and LFW.<sup>[31]</sup> However, most of the residual stress investigations carried out on EBW and LFW have focused on joining the same titanium alloy, with only a few looking at joining dissimilar titanium alloys. Xie *et al.*<sup>[32]</sup> investigated residual stress in a LFW joint between a  $\beta$  processed Ti-17 and an  $\alpha + \beta$  processed Ti-17, using the contour and the X-ray diffraction (XRD) methods. The results showed an initial asymmetric tensile peak in the joint with a 440 MPa magnitude on the  $\beta$  Ti-17 side, a 350 MPa on the  $\alpha + \beta$  Ti-17 side, and a stress of 200 MPa at the center of the weld. Bandyopadhyay *et al.*<sup>[33]</sup> joined Ti-64 to Ti-5553 using LFW and used the

energy-dispersive XRD method to characterize the residual strain in the bond. Again, a peak was observed across the bond with a higher strain in Ti-5553. However, this residual stress peak was reduced after further heat treatment.

There are a limited number of investigations measuring residual stress generated during the consolidation of powder using FAST or HIP routes. The residual stress measurements carried out on the more established HIP process can be used as a reference for FAST processed material as the cooling and unloading stages are very similar. Li *et al.*<sup>[33,34]</sup> predicted potential residual stress in HIP caused by thermal stresses due to non-uniform densification of the powder. The heat source in HIP is surrounding the canned powder, which can lead to quicker densification of the external powder layers. This external layer, termed the “densification wave”, can support the load that creates this non uniform densification. It was observed that the unloading of the sample is the critical stage for the generation of residual stress. To reduce the residual stress level during the unloading stage, the pressure and temperature were closely monitored to allow for stress relaxation to occur. These observations agree with the predictions proposed by Bahei-El-Din *et al.*<sup>[35]</sup> whereby the cooling rate was classed as the most influential parameter on the residual stress profile. Nevertheless, the effect of the pressure was only significant when the cooling rate was higher than 1 °C/s. In addition, the prediction showed that the HIP dwell time had little effect on residual stress. Parker *et al.*<sup>[36]</sup> measured the residual stress in Inconel 718 joined to tungsten through HIP using XRD. It was measured that the residual stress in the axial and hoop directions were relatively low compared to the yield stress of the materials (190 and 160 MPa, respectively).

There have been a couple of investigations on residual stress generated through FAST during the consolidation of tantalum and ruthenium. Angerer *et al.*<sup>[37]</sup> compared the residual stress generated by FAST and HP of a sample made of tantalum. They showed that there was no difference in the stress profiles of the two processing routes, with both samples showing a compressive stress normal to the component and tensile parallel to the component. The exact same approach was applied to ruthenium<sup>[38]</sup> where in this case, FAST reduced the residual stress compared to HP due to the more rapid grain growth in the FAST material. A recent study by Childerhouse *et al.*<sup>[39]</sup> showed a relatively low residual stress at a depth of 250  $\mu\text{m}$  for a titanium sample processed with FAST. In addition to this, there has been several studies that have looked at residual stress formation in ceramics. Szutkowska *et al.*<sup>[40]</sup> observed a decrease of residual stresses when increasing the temperature 100°C. Furthermore, the study shows different values of residual stresses for the phases  $\alpha\text{-Al}_2\text{O}_3$  and  $\text{Ti}(\text{C}_{0.5}, \text{N}_{0.5})$ , which is similar to the results obtained by Yu *et al.*<sup>[41]</sup> and Tamanna *et al.*<sup>[42]</sup> The difference in the residual stress between the phases in these cases is due to a different thermal coefficient of expansion.

As yet, there has been no investigation into the development of residual stress when applying FAST for diffusion bonding between two different titanium alloys.

In general, the technologies used to fully densify powder create low residual stress levels. However, FAST offers several advantages over HIP and HP processes. Guillon *et al.*<sup>[43]</sup> stated that it is easier to control the sintering conditions with FAST, as it is faster and promotes high reproducibility. Furthermore, Suarez *et al.*<sup>[44]</sup> mentioned that FAST can densify the powder without coarsening the microstructure due to the high heating rate obtained. Another benefit of FAST over HIP technology is that shaped graphite molds can be used multiple times, as opposed to HIP where powder is encapsulated in a mild or stainless steel can. FAST technology therefore provides manufacturers an opportunity to achieve near net shape parts from powder. The aims of this paper are (i) firstly, to investigate the development of residual stress during the bonding of two dissimilar titanium alloy powders through the FAST process, and (ii) secondly, to explore the evolution of residual stress in bonds of near-net shape components during subsequent hot forging, using the FAST-*forge* route.

## II. METHODOLOGY

### A. Materials

A total of four titanium alloy powders were used in the primary study: Ti-6Al-4V (Ti-64), Ti-6Al-2Sn-4Zr-2Mo (Ti-6242), CP-Ti and Ti-5Al-5V-5Mo-3Cr (Ti-5553). The powders were from a range of different sources and powder processing routes; (1) The Ti-64 was PREP powder supplied by TIMET, (2) the Ti-6242 was EIGA powder supplied by Carpenter LPW, (3) the CP-Ti was hydride-dehydride (HDH) powder from Phelly Materials Inc., and (4) the Ti-5553 powder was gas atomized from a forged billet by TLS Technik Spezialpulver. For the near-net shape eye-bolt FAST-DB forging, Ti-64 HDH powder with an ASTM B348-11 Grade 5 chemistry was used.<sup>[13]</sup> The particle size distribution (PSD) was measured using a Malvern Mastersizer 3000 laser diffraction particle size analyzer with a wet dispersion method. A total of 20 measurements were done for each powder and the results are shown in Figure 1.

### B. Experimental Procedure

The as FAST samples were made at the University of Sheffield using an FCT Systeme GmbH SPS Furnace Type HP D 25. The temperature was measured with a pyrometer 3 mm away from the interface between the powder and the upper punch. The powder was introduced into a graphite ring mold that was lined with graphite foil to avoid bonding between the powder and the mold. A 3D printed polymer divider in the shape of a cross was used to separate the different titanium alloys in the mold. The cross shape restricted the movement of the divider and allowed to keep a straight bond when the divider was removed. For the as-FAST material, half of the mold was filled with one titanium alloy powder and the other half with a different alloy powder. Then, the powder charge was flattened at each side and the divider

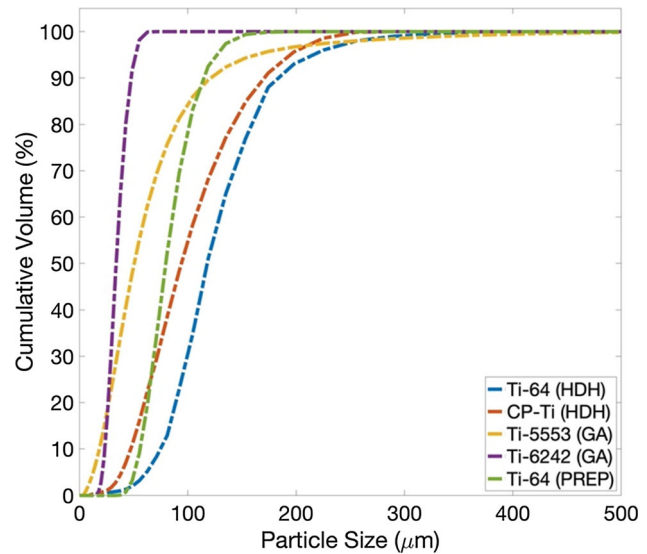


Fig. 1—Particle size distribution (PSD) graph of the powder used in this work represented as a cumulative volume.

was carefully removed to retain a straight bond line, as shown in Figure 2(a). Once the multi-powders were set in the mold, it was then processed through FAST. To limit oxygen pick up, the process was carried out under vacuum.

Two samples were made for each of the FAST-processing parameters for residual stress characterizations, i.e., one sample was analyzed by XRD and the other by the contour method. For FDB3 bond, only one sample was made, and it was analyzed with XRD. A total of four different processing parameters were used to produce the as FAST material (see Table I). The dwell temperature used during processing was 30 °C higher than the highest  $\beta$  transus of the alloys processed, the only exception was FDB3. At the end of the dwell, the sample was left to cool inside the furnace and the pressure decreased from 35 MPa to 5 MPa during the first minute of the cooling cycle. Figure 2 illustrates the three processing steps carried out for each sample and what orientations of the samples were characterized using both the XRD and the contour methods.

The FAST-*forge* components were hot forged from preform bars made of two different titanium alloys. To machine these bars, it was necessary to create a 250 mm FAST billet, as shown in Figure 3. The FAST processing was carried out on the larger FCT System GmbH SPS Furnace Type H-HP D 250 at Kennametal UK Ltd., in Newport, South Wales, UK. The procedure to fill the graphite ring mold with titanium powder was the same as that used for the smaller FAST samples. The main difference was the distribution of the two alloys inside the mold, as shown in Figure 3(a). Table I presents the parameters used for processing of the powder combinations. The next step was to machine the surface of the as FAST billet to remove the graphite layer and determine the position of the bond across the billet. Then, the preform bars were machined parallel to the bond as shown in Figures 3(c), (d).

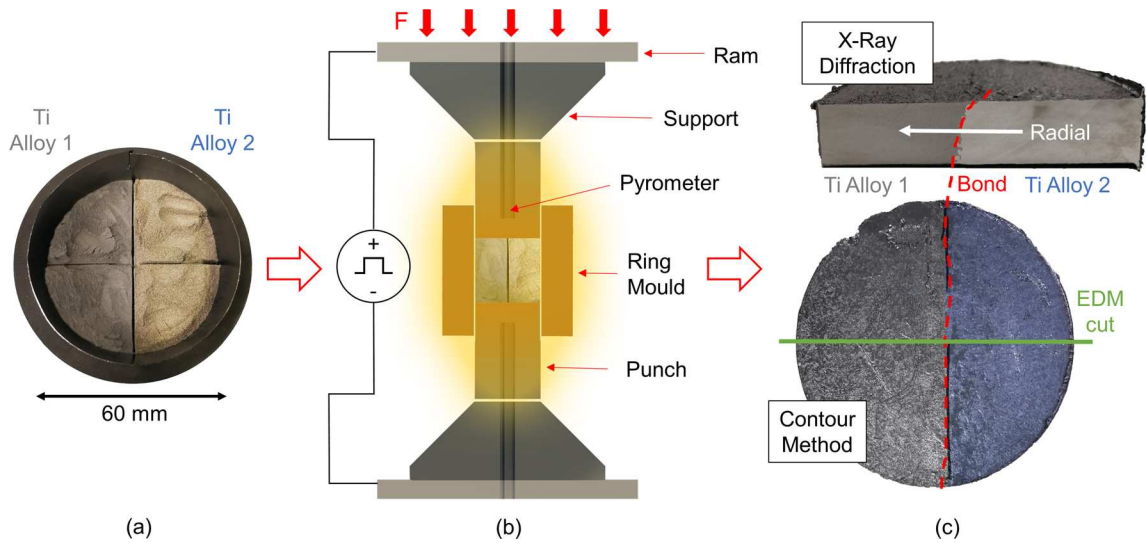


Fig. 2—(a) Photograph of the two titanium alloys powders in the graphite ring mold after removing the dividers. (b) Schematic cross-sectional view of a FAST machine. (c) Photograph of the samples after being process with FAST. The top sample in (c), sectioned in half, shows the trajectory of the locations where the XRD residual stress profiles were measured, and the bottom sample shows the location of the EDM cut for the contour method.

**Table I. Summary of the FAST-Processing Parameters for Each Sample.**

			FAST Processing Parameters				
Name	Diameter (mm)	Materials	Heating Rate (°C/min)	Pressure (MPa)	Dwell Temperature (°C)	Dwell Time (min)	Cooling Rate (°C/min)
As FAST	F1	Ti-64	100	35	1030	20	63
	FDB1	Ti-64 /	100	35	1030	20	63
		Ti-6242					
	FDB2	CP-Ti /	100	35	930	20	63
FDB3	Ti-5553						
	CP-Ti /	100	35	1000	20	63	
FAST-forge	FF1	Ti-64 /	25	35	1200	60	9
		Ti-5553					
	FF2	Ti-64 /	25	32.5	1030	60	9
		Ti-6242					

The closed die hot forging was conducted at W.H. Tildesley, Wolverhampton, UK, on a Massey 1.1 MSC drop hammer forge with foot pedal control and 11 kJ blow energy. The preforms were heated with a gas furnace to a temperature below the  $\beta$  transus and the dies were heated to minimize any die chilling effects. At the end of the forging process, the flash was crimped off and the components were water quenched. Figure 3(e) shows the preform bar after one hammer blow and Figure 3(f) shows one of the two near-net shape geometries analyzed in this study. Further details of the eye-bolt FAST-DB forgings can be found in Reference 13.

### C. Residual Stress Measurements

The residual stress measurements were carried out in the bond using XRD and the contour methods. The points for the XRD measurements traversed across the

bond, as shown in Figure 2(c). Additionally, Figure 2(c) also shows the direction of the EDM cut for the as FAST material and Figure 4 shows those for the forged components.

#### 1. X-ray diffraction

The equipment and method used to measure residual stress with XRD was a Proto LXR Stress Diffractometer and the  $\sin^2\psi$  method in accordance with the NPL's good practice guide.<sup>[45]</sup> Two anode targets were used for the acquisition of the diffraction patterns from different crystallographic planes. For the  $\alpha$  and  $\alpha + \beta$  alloys, a copper anode target with a wavelength of 1.54 nm was used to measure the diffraction peak from the  $\{2\ 1\ 3\}$  crystallographic plane. For the metastable  $\beta$  alloy, a vanadium anode target with a wavelength of 2.50 nm was used to measure the diffraction peak for the  $\{2\ 1\ 1\}$  crystallographic plane. A nickel filter was used to protect the detectors when using the copper anode

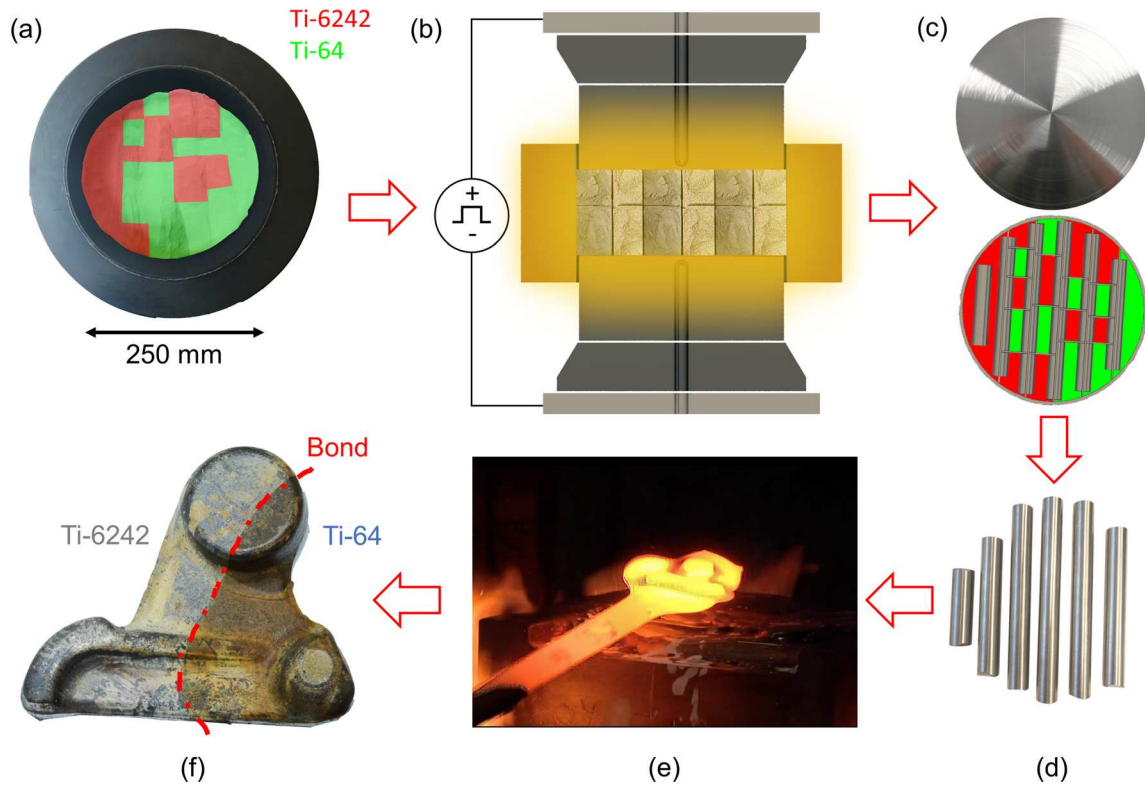


Fig. 3—(a) Photograph showing the distribution of the powders in the graphite ring mold. (b) Schematic cross-sectional view of a FAST machine. (c) Photograph and CAD design of a disk after processing with FAST with the location of the preforms and their distribution with respect to alloy type shown. (d) Photograph of the forging preforms machined from the disk. (e) Photograph of the FAST-DB rocker arm forged after the first hammer blow. (f) Photograph of a rocker arm near-net shape component.

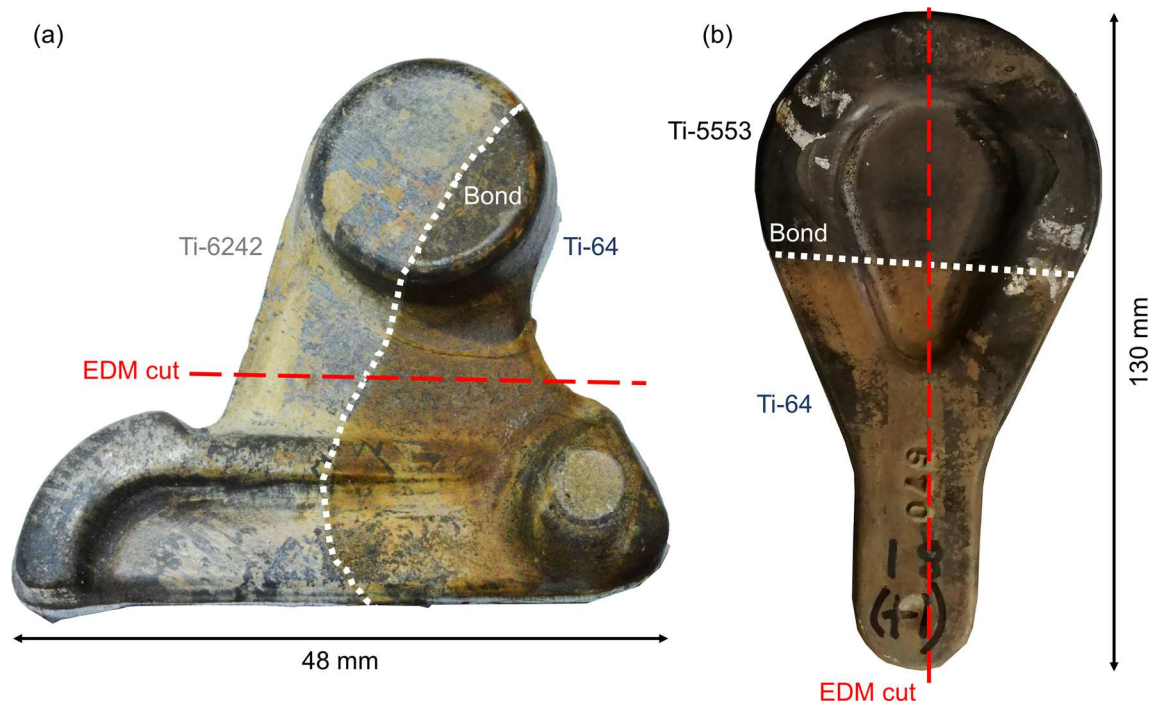


Fig. 4—Photographs of the two final FAST-DB near-net shape forged components with the location of the EDM cut for residual stress measurement using contour method highlighted. (a) Rocker arm, and (b) eyebolt.

**Table II. Summary of the Mechanical Properties Used for the Calculation of Residual Stress by XRD.**

	CP-Ti	Ti-6242	Ti-64	Ti-5553
Young's Modulus (GPa)	105	111.5	114	110
Poisson's Ratio	0.37	0.32	0.342	0.285

target. For the FDB2 and FDB3 materials, the XRD stress measurements were carried out across the bond with one anode (i.e.,  $\alpha$  or  $\alpha + \beta$  side), and then repeated with the second anode (i.e., the metastable  $\beta$  side).

The data were combined with the bond as a reference. The stresses were calculated from the strains of the {2 1 1} and {2 1 3} Bragg reflections assuming the Young's modulus and the Poisson's ratio summarized in Table II for each material. The Bragg's angle varied for each alloy, including 139.69 deg for CP-Ti and Ti-6242, 142 deg for Ti-64, and 145 deg for Ti-5553. The measurements were conducted at two orthogonal directions of axial and hoop at each point. A total of 10 profiles were characterized for each measurement with an exposure time of 4 s per profile. The beta angle varied between 0-30 deg for axial measurements and 0-25° for radial measurements. The oscillation of the beta angle was  $\pm 3$  deg and the round collimator used had an aperture size of 1 mm diameter. For the FAST material, the samples were first sectioned in half with a Secotom-20 and then electropolished with a Struers Lectropol-5 electrolytic polisher to ensure that there was minimal residual stress generated from the mechanical cut. The XRD stress measurements were then conducted, in-plane, on the electropolished cut surface in the XX direction. The number of points measured varied for each sample.

### 2. Contour method

The contour method, developed by Prime,<sup>[46]</sup> was used to measure the residual stress across the plane of several bonds. First, the samples were sectioned, in the direction of the plane of interest (see Figures 2 and 3), using electrical discharge machining (EDM) to minimize cut induce surface damage. The equipment used to section the sample was the Agie Charmilles CUT 400 Sp Electrical. The cut was done with a 0.25 mm brass wire with a steady rate, and the samples were clamped appropriately as close as possible to the cutting plane from both sides to ensure a stable cut and eliminate rigid body motion. For each sample, the two sectioned planes (i.e., half cuts) were then scanned with an Alicona Infinite Focus IFM G4 to map the surface. The Alicona scans were conducted at  $5 \times$  magnification using a  $1 \mu\text{m}$  vertical resolution and  $10 \mu\text{m}$  lateral resolution. The acquired surface profiles were then cleaned by removing all the outline points and noise. The data from both halves were aligned and, and they were then linearly interpolated onto a common grid, after which the two sets were averaged. These were done using an in-house developed software in MATLAB®.

For the evaluation of residual stress, due to the small size of the components, it was necessary to build a 3D finite element (FE) model of the parts. A GOM ATOS TripleScan III was used to create the 3D models for the FE. with the models were then imported to Abaqus™ and the simulations were carried out assuming isotropic elasticity with the Young's modulus and Poisson's ratios presented in Table II, and the averaged surface profiles. The bond between each two alloys with their respective mechanical properties were defined in the 3D models. The simulations were done with an element spacing of 0.2 – 1 mm on the cut surface, using C320R element type. The residual stress was evaluated by the FE software by forcing the cut surface into the opposite shape of the averaged contour data.<sup>[28,47]</sup>

### 3. Analysis techniques

For microstructural analysis, samples were metallographically prepared using progressively finer grit SiC grinding paper. The final polishing stage was conducted with a Struers MD-Chen and  $0.06 \mu\text{m}$  colloidal silica combined with 10 pct concentration hydrogen peroxide. All the metallographic procedures were carried out with a Struers Tegramin-25. The microstructures of the titanium alloys were observed with a Nikon Eclipse LV150 optical microscope and an FEI Inspect F50 scanning electron microscope (SEM).

Elemental analysis, via point scans, were conducted using a X-EDS system, interfaced to a Philips XL30 SEM. The detector was first calibrated with a sample made of pure cobalt to obtain quantitative data for each point. The points were linearly spaced perpendicular to the bond over 10-30  $\mu\text{m}$  distance, depending on the diffusion rates of the elements. Each line scan had 15-20 points and a total of 3 scans at different locations were completed for each sample. The dwell time for each point was varied between 1.5-2 mins. This time was sufficient to obtain quality data without compromising processing time. The length of the scans was long enough to obtain the full diffusion profile for each bond. The data were plotted using MATLAB® software and the fitting of the points were obtained with the curve fitting app in the same software.

The hardness profile was obtained with a Struers Durascan 70 G5 which has automatic hardness evaluation. A total of 100 indentations was perform across each bond combination. The indentations were distributed in five rows with 20 indentations in each and the dwell time for each indentation was 15 s, which abides by the ASTM E384 standard. Each row crossed the bond diagonally to evaluate more points in the proximity of the bond, increasing the resolution of the hardness change across the diffusion bond. The microhardness load was 9.81kgf for all samples, except for the bond between CP-Ti/Ti-5553 for which 1.962kgf was applied. The distance from the indent to the bond was measured from micrographs taken by optical microscope using ImageJ,<sup>[48]</sup> and the data were plotted with MATLAB®.

### III. RESULTS AND DISCUSSION

#### A. Fast Material

##### 1. Microstructure

The microstructure of the samples produced using FAST for this study are shown in Figure 5. The primary observations are that F1 and FDB1 have reached a densification of 99.98 pct and no porosity is visible in Figures 5(a), (b). However, the FAST-DB samples FDB2 and FDB3 have some visible porosity, especially in the Ti-5553 region, as shown in Figure 5(c), (d). The final density for Ti-5553 in FDB2 and FDB3 is 99.82 and 99.40 pct, respectively. Yet, the final density in CP-Ti for FDB2 and FDB3 is 99.92 pct in both cases. It is possible to obtain a higher densification for Ti-5553, as shown by Pope *et al.*,<sup>[14]</sup> however, the temperature used in this work was not high enough to remove all the porosity in these powders. Nevertheless, this small amount of porosity should not affect the residual stress measurements of the FAST material.

The F1 sample has a classic fully transformed, large equiaxed grain structure (300-500  $\mu\text{m}$ ). The sample was

cooled from 1030  $^{\circ}\text{C}$  with an average cooling rate of 63  $^{\circ}\text{C}/\text{min}$ , which created a relatively fine  $\alpha$  laths with an average width of 2  $\mu\text{m}$ . The same microstructure was also achieved for the FDB1 sample in the Ti-64 region, as the processing conditions were the same. The Ti-6242 side in FDB1 also has a classic fully transformed, large equiaxed grain structure but the size of the grains is slightly smaller (200-300  $\mu\text{m}$ ) and the average width of the  $\alpha$  laths is 1.5  $\mu\text{m}$ . The bond between the two alloys has a smooth transition from the darker Ti-64 alpha colonies to the brighter ones in Ti-6242. Furthermore, there is no noticeable changes in the secondary alpha size or morphology, as shown in Figure 5(b). The change of brightness (Z contrast) between the two alloys in the micrographs is due to the higher atomic weights of the elements in the Ti-6242 alloy, such as Zr and Sn.

The microstructures in FDB2 and FDB3 in Figures 5(c), (d) are very similar with the main difference between them being the temperature at which they were processed. The CP-Ti microstructure consists of a large grain size with plate like substructures while the microstructure of Ti-5553 consists of large prior  $\beta$

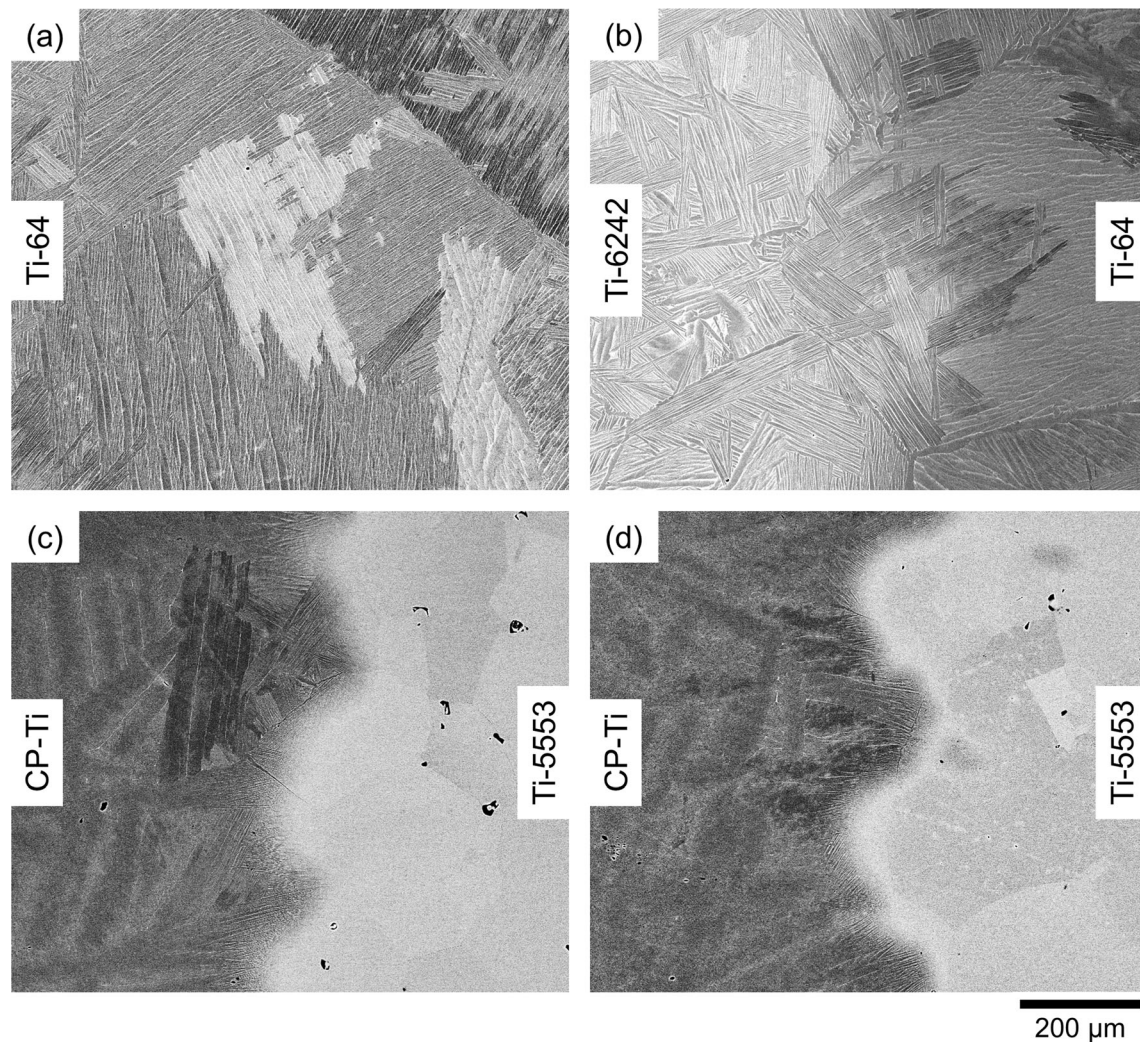


Fig. 5—Backscatter electron micrographs of the as FAST samples for (a) Ti-64 (F1), (b) Ti-6242 / Ti-64 (FDB1), (c) Ti-5553 / CP-Ti (FDB2), and (d) Ti-5553 / CP-Ti (FDB3).

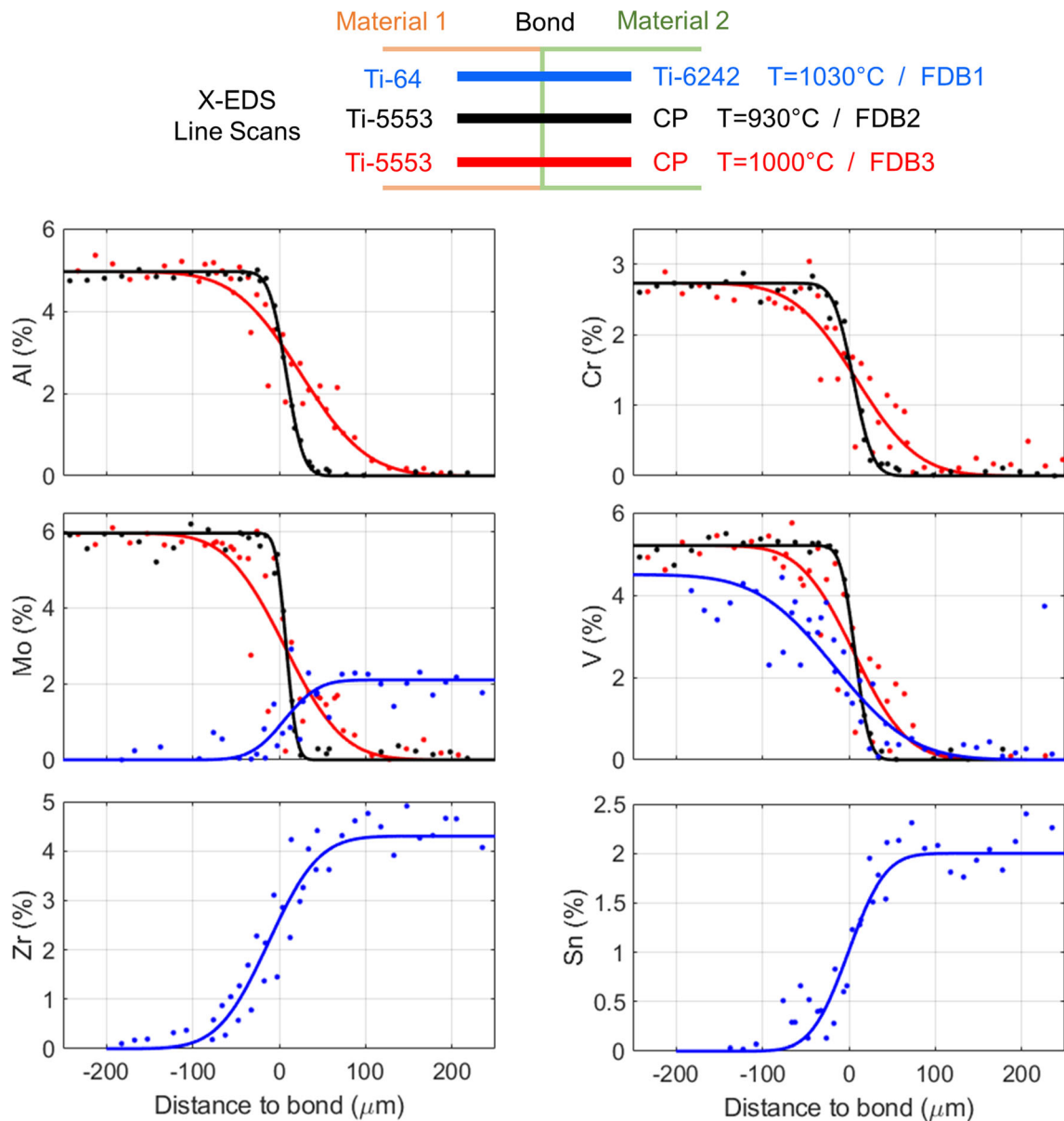


Fig. 6—Diffusion profiles of the six elements which make the titanium alloys Ti-64, Ti-5553 and Ti-6242. Each color in the graph represents the diffusion profile across the bond of one FAST-DB sample (Color figure online).

grains in both samples (100 to 300  $\mu\text{m}$ ). The bond between the two alloys transitions from an  $\alpha$  alloy to a  $\beta$  alloy, which creates a microstructure with the formation of  $\alpha$  laths and fine secondary  $\alpha$ .<sup>[14]</sup>

### 2. Diffusion profiles

The results of elemental analyses for the evaluation of diffusion profiles for the three bonds (FDB1, FDB2 and FDB3), measured by X-EDS, are shown in Figure 6. The diffusion of the elements across the bond for all the samples is small compared to standard joining conditions where the HAZ can reach millimeters scale. The length of the diffusion zone across the bond was used to determine if the measured residual stress was due to chemical misfit across the bond.

For FDB1, the element with higher diffusion rate is vanadium with an approximate diffusion of 220  $\mu\text{m}$ . Meanwhile, for FDB2 and FDB3 the element with higher diffusion is aluminum with an approximate diffusion of 270  $\mu\text{m}$ . FDB3 has significantly higher diffusion of the elements compared to FDB2 due to their respective processing temperatures. Overall, it is safe to assume that for the three FAST-DB samples, the diffusion zone across the bond was less than 300  $\mu\text{m}$ .

### 3. Microhardness profiles

The plots of microhardness profiles across the bond for the three FAST samples are shown in Figure 7. Figure 7(a) shows the hardness of FDB1, which has a bond made of two similar titanium alloys. Meanwhile,

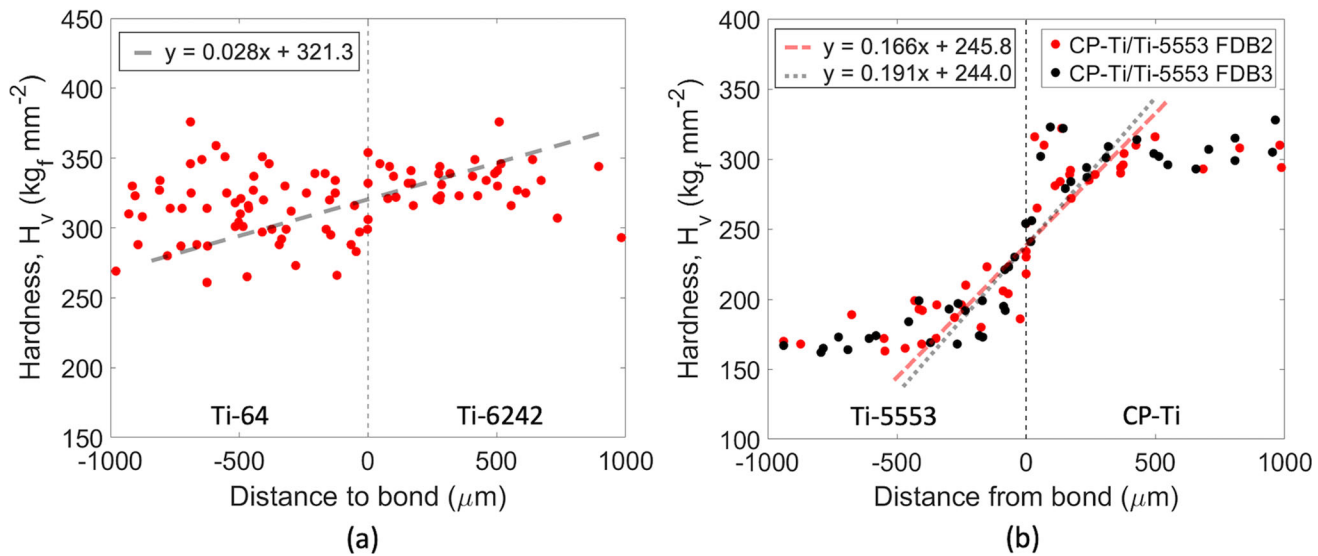


Fig. 7—Plots of hardness profiles for diffusion bonds in (a) FDB1, (b) FDB2, and FDB3.

Figure 7(b) presents the hardness of FDB2 and FDB3, which have a bond made of contrasting types of titanium alloys.

The hardness profile across the bond in FDB1 shows an increase in hardness from Ti-64 to Ti-6242. Although the increase of hardness is small, this change follows the linear regression represented by  $y = 0.028x + 321.28$ . On the other hand, the hardness across the bond in FDB2 and FDB3 present a clear transition between CP-Ti and Ti-5553. CP-Ti bulk material has an average hardness of 160Hv while Ti-5553 has an average value of 300Hv. Therefore, the hardness increases steadily from the alloy with the lower hardness to the one with the higher hardness (or vice versa). The linear regression equation of FDB2 is  $y = 0.166x + 245.8$  while the equation for FDB3 is  $y = 0.191x + 244.02$ . Therefore, it is clear that the difference between both samples is minimum and the difference in the diffusion profiles between FDB2 and FDB3 observed in Figure 6 seems to have a little effect on hardness across the bond. In comparison with the results obtained by Pope *et al.*,<sup>[14]</sup> a peak of hardness in the bond region has not been observed. Note that the points used to calculate the linear regression are only the ones that are less than 500  $\mu\text{m}$  away from the bond to only capture the diffusion bond.

#### 4. Residual stresses measurements

The contour method of residual stress measurement was utilized to obtain full 2D map of out-of-plane of the cut (i.e., EDM wire cut surfaces) residual stress component to provide understanding of process-induced residual stress distribution. Since the uncertainties associated with the stresses measured by the contour method are significantly high close to the edges, owing to the nature of the measurement method, the XRD stress measurements were carried out on the surfaces for a more precise assessment of residual stress on the surface and across the bonds.

Figure 8(a) through (c) show the results of residual stress measurements by the contour method on the as FAST materials, including Ti-64 monolithic (F1), Ti-64 with Ti-6242 (FDB1) and CP-Ti with Ti-5553 (FDB2), respectively. The measured stress distributions for all samples appear to be very similar, with relatively low stress magnitudes, where the core of the samples contain compressive stress and the outer skirts of the samples tensile. The contour method has not picked up a recognizable pattern at the interface between different materials in the location of the bond for samples FDB1 and FDB2. This can be due to the very small size of the interface since the diffusion in the bond was very small, i.e., in the order of 200  $\mu\text{m}$  for FDB1 and 50  $\mu\text{m}$  for FDB2, which resulted in smaller scale residual stresses (i.e., Type II and III) that cannot be resolved by the contour method. Additionally, the materials joined in this case have very similar elastic properties, which are in the main parameters in the calculation of residual stress by the contour method (i.e., isotropic elasticity).

Owing to the nature of the stress measurements by XRD technique, which relies on the measurement of lattice strain in a non-destructive manner, has a rather higher resolution with sensitivity to lower scale residual stresses. Nevertheless, to measure the residual stress across the bond the XRD was used. To capture the stress at the interface, sequential overlapping scans were performed from one side of the interface to another through the bond.

Figure 9 shows the residual stress profiles measured by XRD for F1, FDB1, FDB2 and FDB3. The results obtained for F1 in Figure 9(a) show very low magnitudes of stress with the highest values in the order of 100 MPa, which correlates well with the results presented in Figure 8(a) measured by the contour method. The measurements across the bond for FDB1 show very low residual stress, similarly to the results of the contour method shown in Figure 8(b). The stress profile at the bond appears to be resolved much better by the XRD

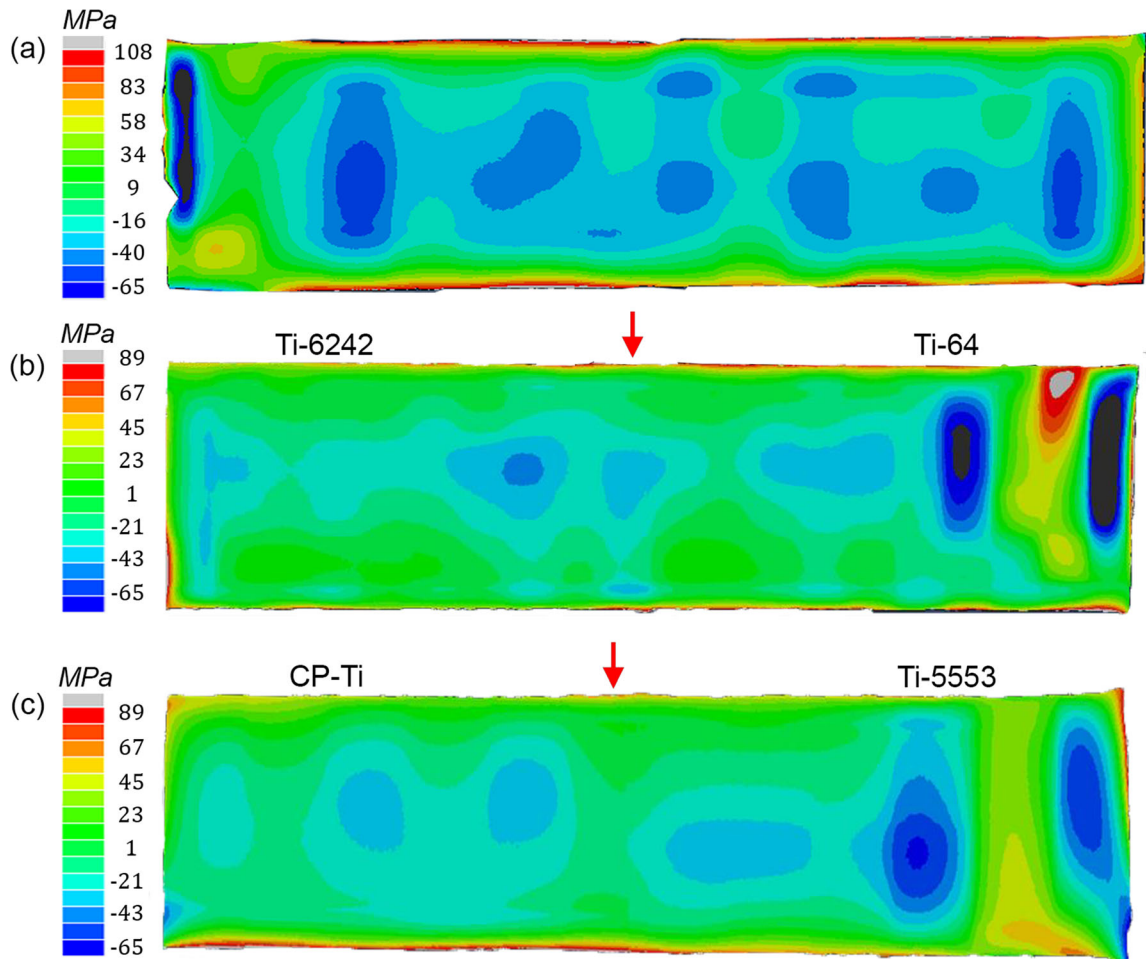


Fig. 8—Out-of-plane residual stress distribution measured by the contour method for (a) Ti-64 (F1), (b) Ti-64 / Ti-6242 (FDB1), and (c) CP-Ti / Ti-5553 (FDB2) bonds.

technique, hence, it is possible to observe a small increase in residual stress in the Ti-6242 region adjacent to the bond. This small peak can be due to a difference in the expansion rate of the materials when cooling the samples from process temperature.

Measurements of residual stress by XRD in FDB2 and FDB3 (CP-Ti/Ti-5553) samples were rather challenging, compared to FDB1 (Ti-64/Ti-6242), because two different target anodes were deployed separately for the materials on each side of the bond. Therefore, Figures 9(c), (d) have separated graphs to construct the stress profile in both the  $\alpha$ -Ti and the  $\beta$ -Ti phases. The results show that for both samples the stress measured in  $\alpha$ -Ti are very low and tend to increase towards the bond. The residual stress in the  $\beta$ -Ti look significantly different for both samples. FDB2 have low residual stress, similarly to that in the  $\alpha$ -Ti. However, FDB3 has moderate to high compressive stress in the bond, reaching magnitudes close to  $-500$  MPa. Additionally, a peak of tensile shear stress in the same location with a value close to  $+300$  MPa was also measured. The significant difference between the measured radial residual stress of FDB2 and FDB3 could be due to various reasons such as dissimilar thermal, plastic deformation

or chemical mismatch.<sup>[20,21]</sup> It is likely that the chemical mismatch, leading to a drastic change in microstructures of CP-Ti and Ti-5553, can be the dominant cause. One of the microstructures that can form in a bond between these two alloys is a fine secondary  $\alpha$  that increases the hardness at the bond, as observed by Pope *et al.*<sup>[14]</sup> The formation of these fine secondary  $\alpha$  in conventional Ti-5553 are due to an aging heat treatment with a temperature ranging within  $400$  °C to  $650$  °C. The size and volume fraction of the  $\alpha$  phase increases when increasing the aging temperatures.<sup>[49]</sup> It has been observed that the  $\alpha$  phase forms within 90 to 120 seconds after reaching the aging temperature for Ti-5553 quenched and aged at  $570$  °C.<sup>[50]</sup> Furthermore, when Ti-5553 is aged at  $600$  °C, the formation of  $\alpha$  can occur after 0 second.<sup>[51]</sup> FDB2 and FDB3 were not subjected to aging heat treatment but the cooling rate was relatively slow ( $66$  °C/min), which could be equivalent to a very short aging process. Only fine secondary  $\alpha$  was observed in the bond location; however, this could also be due to the local alloy chemistry produced in the bond. For example, Manda *et al.*<sup>[52]</sup> observed that the  $\alpha$  phase precipitation was easier for chemistries with lower formation energy/atom values. The precipitation of the

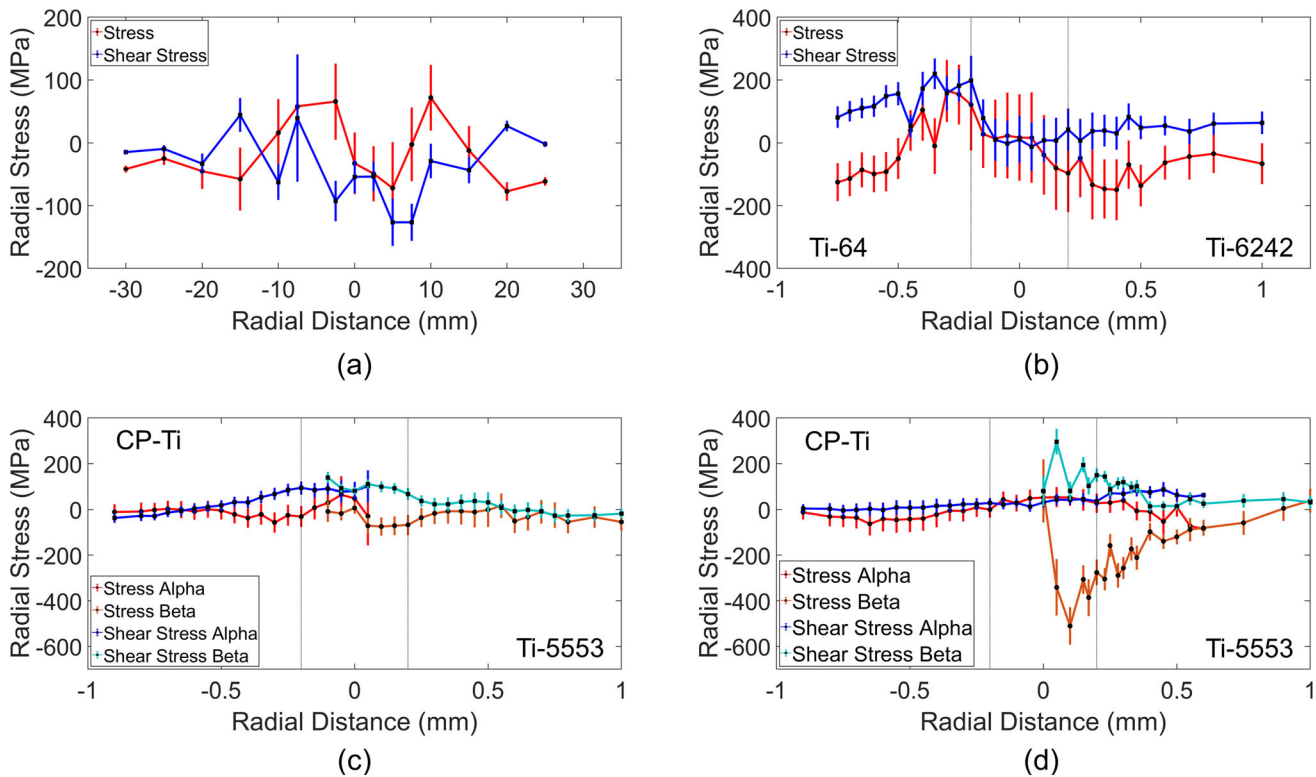


Fig. 9—Plots of radial residual stress measured by XRD in (a) Ti-64 (F1), (b) Ti-64 / Ti-6242 (FDB1), (c) CP-Ti / Ti-5553 (FDB2), and (d) CP-Ti / Ti-5553 (FDB3).

$\alpha$  in the  $\beta$  matrix can produce residual strains in the microstructure, as pointed out by Zheng *et al.*<sup>[51]</sup> These residual strains can be produced because a short aging heat treatment will not produce a thermodynamically stable microstructure. Therefore, it is likely that the interface between the two phases is not fully coherent, which leads to the generation of small- to meso-scale (e.g., grain boundary stress) residual stresses than can be resolved by XRD.

The samples tested by Pope *et al.*<sup>[14]</sup> were processed at 1200 °C, which is 200 °C to 270 °C higher than the temperature used to process the samples in this case. Although the hardness profile in Figure 7 does not show a peak of hardness in the bond for any of the samples, fine secondary alpha has been observed in the bond for FDB2 and FDB3, as shown in Figures 10(a) and (b) respectively. One possible reason why the hardness does not show a peak is because the region with fine secondary alpha is only 10  $\mu\text{m}$  for FDB3 [Figure 10(d)] and even smaller for FDB2 [Figure 10(c)], which were not captured by the micro indentations.

The XRD method used to measure the residual stresses across the bond consisted of overlapping the different scans analyzed in the sample, as explained in the methodology. One of the issues with measuring the stresses in this manner, is that the final values must be averaged between the multiple overlapping measurements. Therefore, it is possible that certain stresses in very small areas have been removed when averaging the values. The diffusion profile for FDB2 is only 50  $\mu\text{m}$  while for FDB3 is 200  $\mu\text{m}$ , as shown in Figure 6. For

this reason, it is a possibility that the peak of residual stresses observed in FDB3 it also occurs in FDB2.

These results show that the technology FAST is capable to produce low residual stresses components when a single or multiple alloys are joined together. However, there are other causes that can produce residual stresses when joining dissimilar alloys, such as chemical strain or thermal mismatch. Based on the results shown in this section, the main drive of residual stresses the diffusion bond of as FAST sample will be the chemical composition produced in the bond. Therefore, the amount of residual stresses when joining different alloys will have to be studied case by case based on the microstructure produced in the bond region. This work has shown the joining of two extreme titanium alloys, such as CP-Ti and Ti-5553. When joining different types of metals or combining metals with ceramics the thermal mismatch can have an important effect.<sup>[53,54]</sup> The thermal mismatch can potentially be minimized by functionally grading the dissimilar alloys to minimize the sudden change in chemistry but further work is required to demonstrate this.

## B. FAST-Forge Material

### 1. Microstructure and hardness characterization

The cross sections of the near-net shaped FF1 (Ti-64/Ti-5553) and FF2 (Ti-64/Ti-6242) components are shown in Figure 11, including micrographs and 2D hardness maps of the bond regions. The bond in the forged component can be divided into two types,

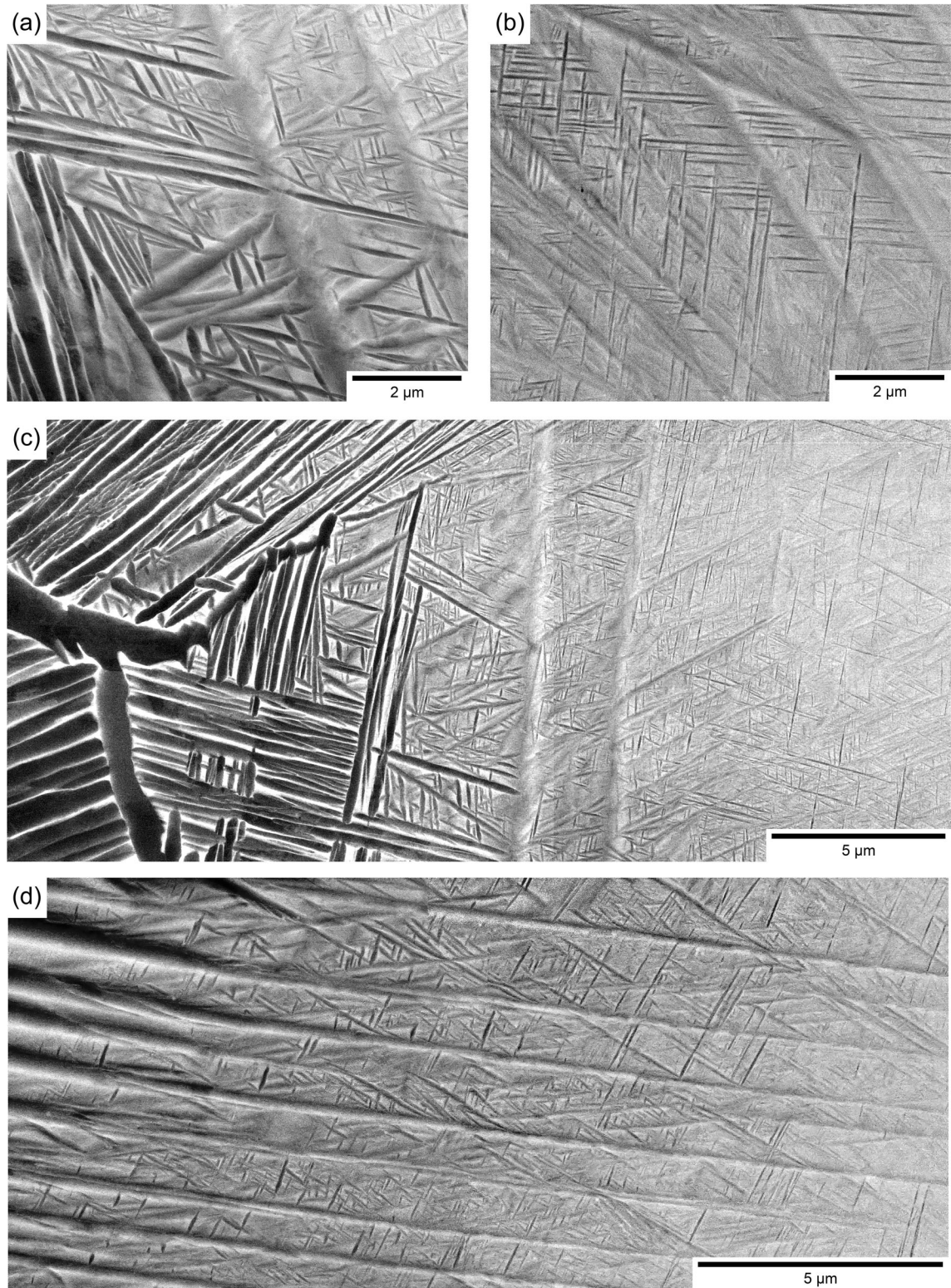


Fig. 10—Backscatter electron micrograph and mosaics at high resolution of the bond between CP-Ti and Ti-5553 for (a), (c) FDB2, and (b), (d) FDB3.

depending on its orientation in the sample; these can be perpendicular or parallel to the forging direction. For FF1, the perpendicular bond (BT1) is shown in [Figures 11(a), (b)] and the parallel bond (BT2) is shown in

[Figures 11(c), (d)]. All the micrographs show a bright and dark region that corresponds to Ti-5553 and Ti-64, respectively.

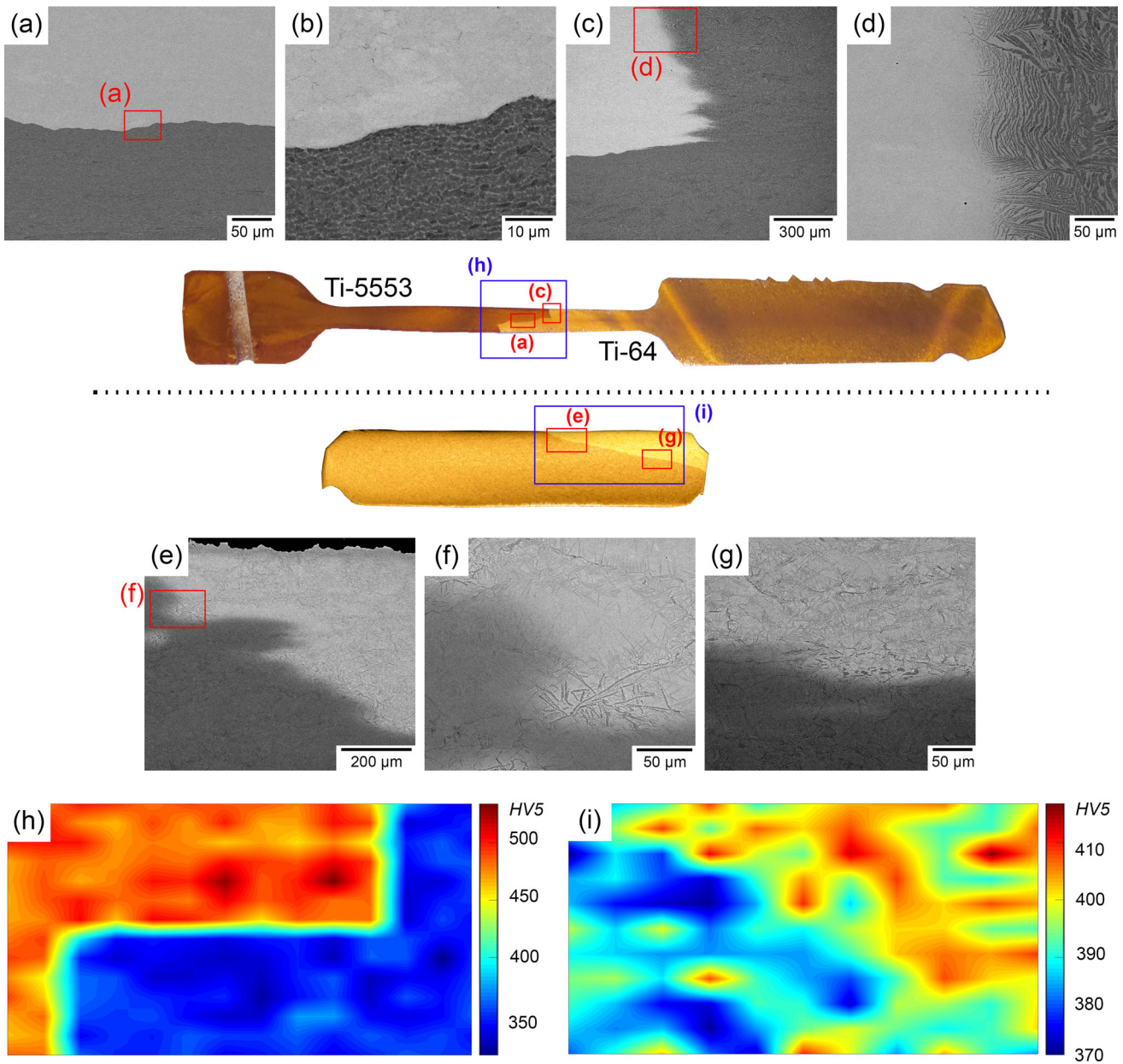


Fig. 11—Backscatter electron micrographs, cross sectional photographs and hardness maps of the FAST-forge components FF1 and FF2. (a) to (d) Micrographs of the component FF1 (Ti-64 / Ti-5553). (e) to (g) Micrographs of the component FF2 (Ti-64 / Ti-6242). Hardness maps of (h) FF1 and (i) FF2.

The micrographs of BT1 shows the grains in Ti-5553 to be slightly elongated perpendicular to the forging direction due to the high strain produced during the forging. There is a lack of clear microstructural features in the micrographs as a result of heating the material above the  $\beta$  transus followed by quenching at the end of the process. The Ti-64 alloy in BT1 has an equiaxed microstructure due to dynamic globularisation mechanism caused by the high strain induced during the forging process.<sup>[55]</sup> It is also observed that the microstructure in the bond has a very sharp transition.

The micrographs of BT2 show the same microstructure for Ti-5553 as that observed in Figure 11(a), but that of the Ti-64 has a deformed Widmanstätten

microstructure. Contrary to BT1, in BT2 there is a transition of the microstructure across the bond, as shown in Figure 11(d). The darker lamellas in Ti-64 tend to get brighter across the bond into the Ti-5553 microstructure. Further details regarding the microstructural evolution during forging and strain distribution across the eye-bolt forging can be found in Reference 13.

The hardness of the bond is shown as a 2D hardness map in Figure 11(h). The bulk material has a hardness around 500Hv for Ti-5553 and 350Hv for Ti-64, which is increased compared to that of the as FAST material shown Figure 7. The hardness across the bond has a smooth transition between both alloys. However, the

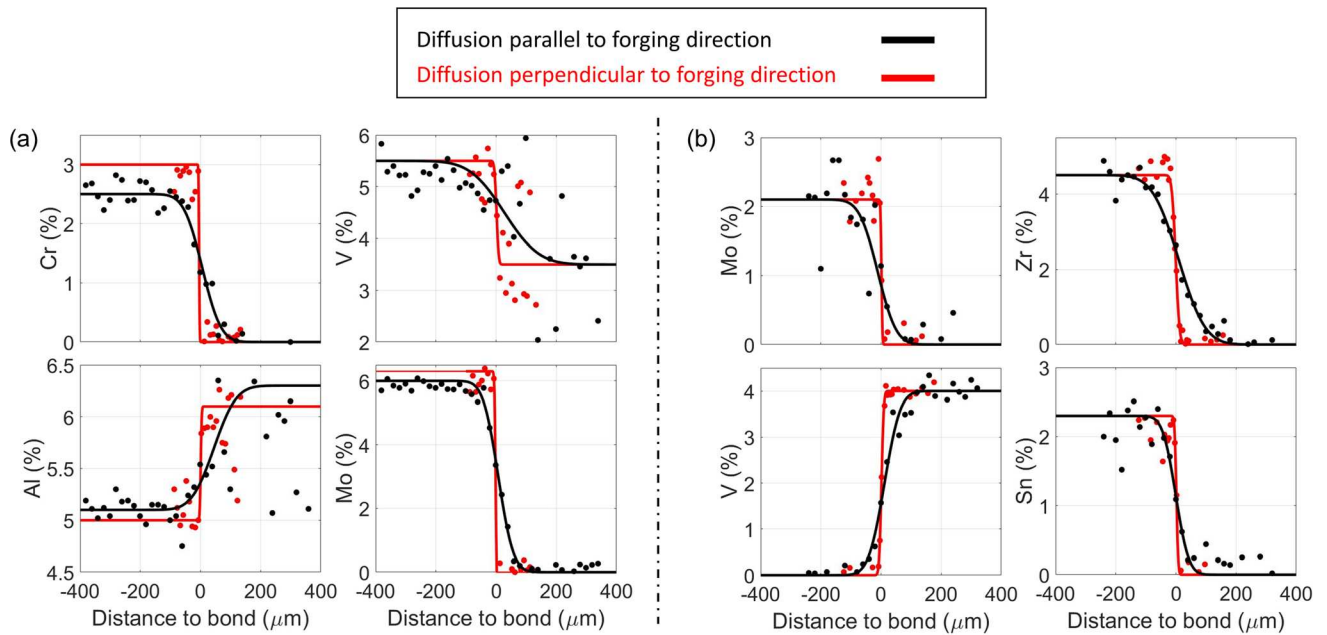


Fig. 12—Graphs of the diffusion profiles of FAST-forge components with the bonds parallel and perpendicular to the forging directions for (a) FF1 and (b) FF2.

change of hardness between the two alloys is longer for BT2 compared to BT1. This cannot be fully appreciated from the 2D map because of the limited number of points that could be tested across the bond as the hardness data were interpolated to create the map.

The FF2 microstructure shown in Figures 11(e) through (g), under the Z contrast of the backscatter electron mode, depicts the Ti-6242 alloy brighter than the darker Ti-64 side. In this case, the location of the bond is in the top right corner of the forged component and the two bond regions are not as well defined as that in FF1. The component has a similar microstructure for both alloys, which consists of a martensitic structure with large parent  $\beta$  grains. These types of microstructures are typical after supertransus forging followed by water quenching. In some areas close to the bond, darker elongated alpha regions have formed, probably due to partial recrystallisation near the bond.

The 2D microhardness map in Figure 11(i) shows that the hardness of FF1 is higher than that of FDB2. The hardness of the two alloys are very similar but Ti-6242 has higher values overall. Furthermore, there is a smooth transition across the bond with no significant increase or decrease of hardness in the adjacent regions.

## 2. Diffusion profile

The diffusion of the two distinctive bond types, BT1 (perpendicular to forging direction) and BT2 (parallel to forging direction), for FF1 and FF2 are shown in Figure 12. For all the measured elements the diffusion is higher in BT2 than in BT1, with an average diffusion distance of 150 and 50  $\mu\text{m}$ , respectively. This correlates well with the results and micrographs presented in Figure 11.

The diffusion in FF1 is higher than FF2 due to the higher processing temperature. Furthermore, in FF1 the element with longer diffusion is vanadium while in FF2 the element with longer diffusion is zirconium.

## 3. Residual stresses measurements

The residual stress in the FAST-forge components were expected to be higher than that in the as-FAST material because of the hot forging and the subsequent water quenching processes. While a high-quality wire-EDM cut was achieved for FF1, that of FF2 was not as clean due to the geometry of the sample and the clamping arrangements during the cut. Meanwhile, the cutting artifacts and the outline points were eliminated from the dataset to minimize their effects on the residual stress evaluation.

The full 2D maps of out-of-plane residual stress for FF1 and FF2 are shown in Figure 13, in which the locations of the diffusion bonds are highlighted by red arrows. The residual stress generated at the bond regions of both components are relatively low, and there seems to be a smooth transition between the dissimilar alloys. Overall, the measured stress in the component can be considered as low to moderate compared to the yield point of the materials.

The FF1 sample has a compressive residual stress at the surface of the Ti-64 region, while the bulk region has tensile residual stress. On the left-hand side of Figure 13(b), the Ti-5553 shows an area under compression which could have been caused by the change in geometry. Furthermore, the higher tensile stress in that same region is an artifact caused by a hole made in the component for self-clamping during the EDM cutting process.

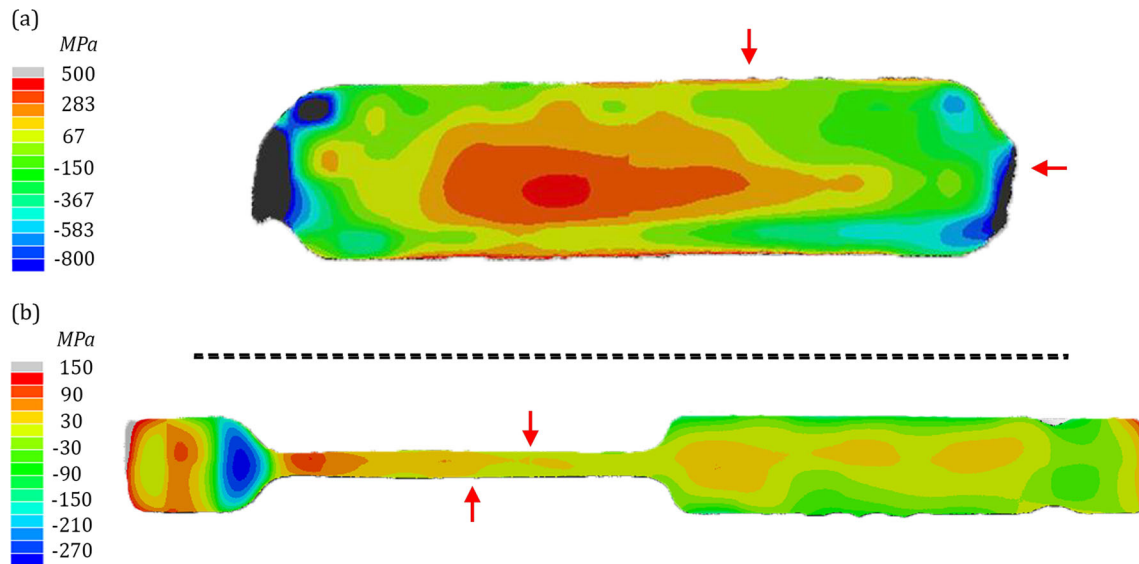


Fig. 13—Contour plots of residual stress distributions for the FAST forged samples (a) FF2 and (b) FF1. The red arrows highlight the locations of the diffusion bond (Color figure online).

The measurements of the residual stress in the bond of FF2 were conducted at the highest strain region, as shown in Figure 4. Figure 13(a) shows higher residual stress in the top right-hand side of the samples. This stress distributions can occur because the bottom left part of the sample was made of Ti-64 and the top part was made of Ti-6242, as shown in Figure 11. Overall, there is high residual stress with a compressive outer layer and a tensile core. Additionally, there is a smooth transition of the residual stress across the bond.

#### IV. CONCLUSIONS

This work has presented, for the first time, the measurements of residual stress distribution in a diffusion bond when dissimilar titanium powders are joined via the FAST process. Furthermore, the residual stress distributions of a near-net shaped components made of dissimilar titanium produced by the two-step FAST-*forge* processing route were also measured and presented. The main outcomes of this study are as follows:

- The use of FAST does not produce defects in the bond for the alloys used. The diffusion of the elements has a maximum distance smaller than  $250\ \mu\text{m}$ . The hardness across the bond for FDB1 does not show significant changes. However, there is a smooth increase of hardness from CP-Ti to Ti-5553 for FDB2 and FDB3.
- The residual stress generated in a component made of a single titanium was very low due to the relatively slow cooling of the sample. All the as FAST samples presented compressive stress in the core and tensile close to the outer layers.
- The diffusion bond of the components showed an increase of the stress profiles towards the interface.

This increase in residual stress is subtle for Ti-64/Ti-6242 (FDB1) but there was a sharper increase for CP-Ti/Ti-5553 (FDB2 & FDB3). It is likely that these stresses are generated by chemical misfit due to the formation of ultrafine secondary alpha in FDB2 and FDB3.

- The FAST-*forge* samples demonstrated compressive stress at the outer layers and tensile at the core, typical of forged and quenched parts. The residual stress was different for the two alloys but there seems to be a smooth transition across the bond.
- The measurements conducted using the contour method lack the resolution to fully characterize the residual stress profile across the bond. However, the XRD method can sufficiently resolve the stresses across the bond, yet there are still limitations to the measurements of very small bonds such as FDB2.

#### ACKNOWLEDGMENTS

This work was supported through the Engineering and Physical Sciences Research Council (EPSRC), grant EP/T024992/1 Doing More With Less. We also acknowledge the EPSRC for funding equipment in the Henry Royce Institute at Sheffield, grant numbers EP/R00661X/1 and EP/P02470X/1.

#### CONFLICT OF INTEREST

On behalf of all authors, the corresponding author states that there is no conflict of interest.

## OPEN ACCESS

This article is licensed under a Creative Commons Attribution 4.0 International License, which permits use, sharing, adaptation, distribution and reproduction in any medium or format, as long as you give appropriate credit to the original author(s) and the source, provide a link to the Creative Commons licence, and indicate if changes were made. The images or other third party material in this article are included in the article's Creative Commons licence, unless indicated otherwise in a credit line to the material. If material is not included in the article's Creative Commons licence and your intended use is not permitted by statutory regulation or exceeds the permitted use, you will need to obtain permission directly from the copyright holder. To view a copy of this licence, visit <http://creativecommons.org/licenses/by/4.0/>.

## REFERENCES

1. V.A. Joshi: *Titanium Alloys: An Atlas of Structures and Fracture Features*, Taylor & Francis, New York, USA, 2006.
2. A.P. Mouritz: *Introduction to Aerospace Materials*, Woodhead Publishing, Cambridge, England, 2012.
3. G. Lutjering and C.W. James: *Titanium*, 2nd ed. Springer, Berlin, Germany, 2007.
4. C. Leyens and M. Peters: *Titanium and Titanium Alloys: Fundamentals and Applications*, vol. 1, Wiley-VCH, Weinheim, Germany, 2003.
5. G. Çam, G. Ipekoğlu, K.H. Bohm, and M. Koçak: *J. Mater. Sci.*, 2006, vol. 41, pp. 5273–282.
6. G. Çam, U. Özdemir, V. Ventzke, and M. Koçak: *J. Mater. Sci.*, 2008, vol. 43, pp. 3491–499.
7. D. Herrmann and F. Appel: *Metall. Mater. Trans. A Phys. Metall. Mater. Sci.*, 2009, vol. 40, pp. 1881–902.
8. X.R. Wang, Y.Q. Yang, X. Luo, W. Zhang, G.M. Zhao, and B. Huang: *Intermetallics*, 2013, vol. 36, pp. 127–32.
9. X.F. Wang, M. Ma, X. Bin Liu, X.Q. Wu, C.G. Tan, R.K. Shi, and J.G. Lin: *Trans. Nonferrous Met. Soc. China*, 2006, vol. 16, pp. 1059–63.
10. M. Holmquist, V. Recina, and B. Pettersson: *Acta Mater.*, 1999, vol. 47, pp. 1791–799.
11. M. Holmquist, V. Recina, J. Ockborn, B. Pettersson, and E. Zumalde: *Scr. Mater.*, 1998, vol. 39, pp. 1101–106.
12. D. He, Z. Fu, W. Wang, J. Zhang, Z.A. Munir, and P. Liu: *Mater. Sci. Eng. A*, 2012, vol. 535, pp. 182–88.
13. J. Pope and M. Jackson: *Metals (Basel)*, 2019, vol. 9, p. 654.
14. J.J. Pope, E.L. Calvert, N.S. Weston, and M. Jackson: *J. Mater. Process. Technol.*, 2019, vol. 269, pp. 200–07.
15. T. Nakamura, K. Hayakawa, S. Tanaka, H. Imaizumi, and Y. Nakagawa: *Mater. Trans.*, 2005, vol. 46, pp. 292–97.
16. N.S. Weston and M. Jackson: *J. Mater. Process. Technol.*, 2017, vol. 243, pp. 335–46.
17. O. Levano Blanch, D. Lunt, G.J. Baxter, and M. Jackson: *Metall. Mater. Trans. A Phys. Metall. Mater. Sci.*, 2021, vol. 52, pp. 3064–82.
18. O. Levano, N. Weston, J. Pope, A. Tudball, D. Lunn, G. Baxter, and M. Jackson: *MATEC Web Conf.*, 2020, vol. 321, p. 03010.
19. S.J. Tuppen, M.R. Bache, and W.E. Voice: *Int. J. Fatigue*, 2005, vol. 27, pp. 651–58.
20. P.J. Withers and H.K.D.H. Bhadeshia: *Mater. Sci. Technol.*, 2001, vol. 17, pp. 366–75.
21. G.E. Dieter: *Mechanical Metallurgy*, 3rd ed. McGraw-Hill Education, New York, 1989.
22. W. Elber: *Fracture Toughness and Slow-Stage Cracking*, 1st ed. ASTM, Philadelphia, 1973.
23. J.D. Almer, J.B. Cohen, and B. Moran: *Mater. Sci. Eng. A*, 2000, vol. 284, pp. 268–79.
24. D. Busse: Cranfield University, 2017.
25. G.S. Schajer: *Practical Residual Stress Measurement Methods*, 1st ed. Wiley, West Sussex, UK, 2013.
26. J.Z. Zhou, S. Huang, L.D. Zuo, X.K. Meng, J. Sheng, Q. Tian, Y.H. Han, and W.L. Zhu: *Opt. Lasers Eng.*, 2014, vol. 52, pp. 189–94.
27. E.J. Fairfax and M. Steinzig: in Conference Proceedings of the Society for Experimental Mechanics Series, Springer International Publishing, New York, USA, 2016, pp. 209–14.
28. W. Rae, Z. Lomas, M. Jackson, and S. Rahimi: *Mater. Charact.*, 2017, vol. 132, pp. 10–9.
29. F. Hosseinzadeh, P. Ledgard, and P.J. Bouchard: *Exp. Mech.*, 2013, vol. 53, pp. 829–39.
30. P. Xie, H. Zhao, B. Wu, and S. Gong: *Exp. Mech.*, 2015, vol. 55, pp. 1329–37.
31. A.R. McAndrew, P.A. Colegrove, C. Bühr, B.C.D. Flipo, and A. Vairis: *Prog. Mater. Sci.*, 2018, vol. 92, pp. 225–57.
32. P. Xie, H. Zhao, and Y. Liu: *Sci. Technol. Weld. Join.*, 2016, vol. 21, pp. 351–57.
33. R. Bandyopadhyay, J. Rotella, D. Naragani, J.S. Park, M. Eff, and M.D. Sangid: *Metall. Mater. Trans. A*, 2019, vol. 50A, pp. 704–18.
34. W.B. Li and K.E. Easterling: *Powder Metall.*, 1992, vol. 35, pp. 47–52.
35. Y.A. Bahei-El-Din and G.J. Dvorak: *Acta Metall. Mater.*, 1995, vol. 43, pp. 2531–39.
36. R.B. Parker, D.W. Brown, and P. Rangaswamy: *Mater. Sci. Forum*, 2000, vol. 347, pp. 229–34.
37. P. Angerer, W. Artner, E. Neubauer, L.G. Yu, and K.A. Khor: *Int. J. Refract. Met. Hard Mater.*, 2008, vol. 26, pp. 312–17.
38. P. Angerer, J. Wosik, E. Neubauer, L.G. Yu, G.E. Nauer, and K.A. Khor: *Int. J. Refract. Met. Hard Mater.*, 2009, vol. 27, pp. 105–10.
39. T. Childerhouse, R. M'Saoubi, L. Franca, N. Weston, P. Crawford, and M. Jackson: *Int. J. Fatigue*, 2022, vol. 163, p. 107054.
40. M. Szutkowska, J. Cyboron, M. Podsiadło, and T. Polczyk: *Ceram. Int.*, 2022, vol. 48, pp. 17116–22.
41. T. Yu, H. Kwon, L. Shi, X. Zhou, D.H. Yoon, P. Tatarko, X. Xu, Z. Huang, and Q. Huang: *J. Eur. Ceram. Soc.*, 2021, vol. 41, pp. 1834–40.
42. N. Tamanna, I.R. Kabir, and S. Naher: *Therm. Sci. Eng. Prog.*, 2022, vol. 31, p. 101283.
43. O. Guillon, J. Gonzalez-Julian, B. Dargatz, T. Kessel, G. Schierning, J. Räthel, and M. Herrmann: *Adv. Eng. Mater.*, 2014, vol. 16, pp. 830–49.
44. M. Suárez, A. Fernández, J.L. Menéndez, R. Torrecillas, H.U. Kessel, J. Hennicke, R. Kirchner, and T. Kessel: *Sinter. Appl.*, 2013, vol. 13, pp. 319–42.
45. M.E. Fitzpatrick, A. Fry, P. Holdway, F. a Kandil, J. Shackleton, and L. Suominen: Measurement Good Practice Guide No. 52. Determination of Residual Stresses by X-Ray Diffraction, 2005.
46. M.B. Prime and A. Gonzales: in Sixth International Conference on Residual Stresses, Los Alamos National Laboratory, 2000, pp. 617–24.
47. J.D. Pollard, S. Rahimi, A. Watford, M. Jackson, and B.P. Wynne: in Proceedings of the 13th World Conference on Titanium, John Wiley & Sons, Inc., Hoboken, New Jersey, USA, 2016, pp. 305–10.
48. C.A. Schneider, W.S. Rasband, and K.W. Eliceiri: *Nat. Methods*, 2012, vol. 9, pp. 671–75.
49. P. Manda, R.M. Samudrala, M.K. Mohan, and A.K. Singh: *Metall. Mater. Trans. A*, 2017, vol. 48A, pp. 4539–52.
50. N.G. Jones, R.J. Dashwood, M. Jackson, and D. Dye: *Acta Mater.*, 2009, vol. 57, pp. 3830–9.
51. Y. Zheng, R.E.A. Williams, G.B. Viswanathan, W.A.T. Clark, and H.L. Fraser: *Acta Mater.*, 2018, vol. 150, pp. 25–39.
52. P. Manda, V. Singh, U. Chakkingal, and A.K. Singh: *Mater. Charact.*, 2016, vol. 120, pp. 220–8.
53. S. Nosewicz, J. Rojek, and M. Chmielewski: *Materials (Basel)*, 2020, vol. 13, pp. 1–21.
54. M. Petrus and J. Wo: *Materials (Basel)*, 2022, vol. 15, p. 1175.
55. B. Kedia, I. Balasundar, and T. Raghu: *Trans. Indian Inst. Met.*, 2018, vol. 71, pp. 1791–801.

**Publisher's Note** Springer Nature remains neutral with regard to jurisdictional claims in published maps and institutional affiliations.